Efficient investigation on fully developed flow in a mildly curved 180° open-channel

Yuchuan Bai, Xiaolong Song and Shuxian Gao

ABSTRACT

Turbulent flow in meandering open channels is one of the most complicated and unpredictable turbulent flows as the interaction of various forces, such as pressure gradient, centrifugal force, and wall shear stresses severely affect the flow pattern. In order to improve significance in engineering application, understanding the overall flow characteristic is the focus. This paper presents the results of numerical and experimental investigations of flow in a 180° mild bend, which is close to criticality with curvature ratio $R/B = 3$. Considering the characteristic of various models, three-dimensional (3D) re-normalization group (RNG) k–ϵ model was adopted to simulate the flow efficiently. Governing equations of the flow were solved with a finite-volume method. The pressure-based coupled algorithm was used to compute the pressure. The flow velocities were measured experimentally with Micro acoustic Doppler velocimeter. Good agreement between the numerical results and measurements indicated that RNG k–ϵ model can successfully predict this flow phenomenon. The flow pattern in this bend is influenced widely by the secondary flow. The variations of velocity components, streamlines, secondary flow, and wall shear stresses are analysed in the study. Some newly discovered phenomenon in this special state are worth noting.

Key words | 180° mild channel bend, experimental model, numerical simulation, secondary flow, turbulent flow

Yuchuan Bai (corresponding author)
State Key Laboratory of Hydraulic Engineering Simulation and Safety,
Institute for Sedimentation on River and Coastal Engineering,
Tianjin University,
Tianjin 300072,
China
E-mail: *ychbai@tju.edu.cn*

Xiaolong Song
Shuxian Gao
State Key Laboratory of Hydraulic Engineering Simulation and Safety,
Tianjin University,
Tianjin 300072,
China

NOTATION

t	time (s)
u	velocity (m s^{-1})
x	streamwise distance (m)
p	pressure (kg m^{-1} s^{-2})
ρ	fluid density (kg m^{-3})
ν	kinematic viscosity (m^2 s^{-1})
ν_t	kinematic eddy viscosity (m^2 s^{-1})
k	turbulent kinetic energy (m^2 s^{-2})
ϵ	dissipation rate of TKE (m^2 s^{-3})
μ	molecular viscosity (kg m^{-1} s^{-1})
S	modulus of the mean rate-of-strain tensor (s^{-1})
h	elevation above bed (m)
r	radial coordinate (m)
τ	wall shear stress (Pa)
y	distance from the wall (m)
U^+	shear velocity (m s^{-1})
k_s	wall roughness (–)
V	velocity vector (m s^{-1})
H	helicity (m s^{-2})
I	strength of secondary flow (m^4 s^{-2})

doi: 10.2166/hydro.2014.108

INTRODUCTION

The flow pattern and sediment transport in meandering open-channel is a hot problem in the field of river dynamics studies. The flow field in channel bends is highly three-dimensional and the flow structure is dominated by secondary flow, which is responsible for higher wall shear stresses and the consequent deposition near the inner bank, erosion near the outer bank. Local deposition or erosion in river bends under the complex flow condition can generate

substantial problems to river regulation structures. Therefore, knowing the characteristics of flow in a channel bend is of great engineering and scientific value.

The spiral motion of water body is initialized by centrifugal forces accelerating water particles near the water surface, which are then transmitted towards the outer bank of the bend. This results in a pressure difference between the outer and inner flow streamline, which is balanced by a near bed flow pointing towards the inner bank of the bend. The superposition of this secondary flow with primary flow forms the so-called helical flow in the bend. Over the years, intensive research works revealed that the direction of the sediment movement in a channel bend is mainly influenced by the helical flow, pointing towards the inner bank near the river bed, and towards the outer bank at the water surface. With the increasing influence of gravity force on the particles, the sediment particles tend to deviate from the flow direction as soon as transversal slope is formed. Then, the balance of sediment distribution is gradually shattered in the process.

The unbalanced consequence of the flow system is mainly rendered in velocity distribution, momentum transportation and energy expenditure. In the past few decades, much research has been devoted to the flow in meandering open channels, both experimentally and numerically. Shukry (1950) was one of the first to study in detail spiral flow of channel bends in the experiment method. Einstein & Harder (1954) studied velocity distribution and the boundary layer at channel bends and indicated that the existence of higher velocities near the outside bank requires, except for the helical flow pattern commonly observed, that the outward flowing upper layers be unaffected by bed shear stress. Soliman & Tinney (1968) developed the theoretical analysis of the head losses in 180° open channel bends and collected experimental data with several flow and bend geometries conditions to check their theory. Kikkawa *et al.* (1973) made experimental investigations on flow at a bend of finite width and compared with theoretical works, which calculated the velocity distribution of secondary flow by taking account of the thickness of the turbulent boundary layer, developing from the outer wall of a channel. Experimental data collected by Thorne *et al.* (1985) in a meandering sand-bed river confirm that the main cell does not stretch to the inner bank in some bends. The flow patterns near the inner half channel depend on the morphology of the channel cross-section. Over the last decade, related researches have become increasingly heated. Ouillon & Dartus (1997) studied flow pattern and shear stress distribution round a groyne in a rectangular channel, based on the combination of experimentation and numerical calculation. Sudo *et al.* (1998) experimentally investigated the turbulent flow in an annular sectioned 90° bend with smooth walls. Their data are very useful for checking the validity of mathematical models of turbulence. Later, Blanckaert & Graf (2001, 2004a), Blanckaert & de Vriend (2003, 2004b) made considerable efforts to measure and investigate the secondary flow. Keevil *et al.* (2006) conducted a series of experiments to study the structure of secondary flow with submarine channels. Through massive experimentation, Abad & Garcia (2009) investigated mean flow and turbulence characteristics to describe bend orientation effects on the hydrodynamics of the flow. Termini & Piraino (2011) carried out research into the evolutionary process of cross-sectional flow along a meandering bend. Their measurements show that a counter-rotating circulation cell takes shape in the upper part near the outer bank, in the case of relative small width-depth ratio.

There exist a large number of flow separation zone and counter-rotating secondary flow cell structure in channel bends. Detailed and accurate descriptions of such flows using physical methods are limited by scale effects (Ramamurthy *et al.* 2012). Computational fluid dynamics (CFD) applications can solve these problems. With the fast development of computer power, various numerical models have been developed to simulate the complex flow structure (Ye & McCorquodale 1998; Olsen 2003; Zeng *et al.* 2008; Van Balen *et al.* 2009; Fischer-Antze *et al.* 2009; Jing *et al.* 2009; Stoesser *et al.* 2010; Abhari *et al.* 2010; Xu *et al.* 2010; Yang & Bai 2011; Li *et al.* 2013). Many researchers used the flow in bends in an attempt to validate their developed CFD code. In one of the successful simulation cases, Wormleaton & Ewunetu (2006) computed outer and inner flow over a fixed naturally geometric bed in a channel bend. Wilson *et al.* (2007) computed the transportation of solute in a large-scale laboratory meandering channel with a self-formed cross-section. They both obtained fairly good agreement with measurements. Moreover, recent literature about real-life case studies of various

contemporary soft computing techniques is appearing in water resources engineering elsewhere, such as Chau *et al.* (2005), Cheng *et al.* (2005), Chen & Chau (2006), Muttil & Chau (2006), Wu *et al.* (2009) and Taormina *et al.* (2012).

The turbulence model is a computational method to close the mean flow equations and solve them, so that a more or less wide variety of flow problems can be computed. There are six known classical turbulence models which are mixing length, standard k–ϵ, renormalization group (RNG) k–ϵ, realizable k–ϵ, Reynolds stress and algebraic stress models (Launder & Spalding 1974). For a meandering channel, RNG k–ϵ model is more appropriate compared with other models due to its ability to precisely capture streamline curvatures at a relatively low Reynolds number. Both the RNG and realizable k–ϵ models have shown substantial improvements over the standard k–ϵ model where the flow features include strong streamline curvature, vortices, and rotation, but the realizable model is still relatively new, it is not clear in exactly which instances it consistently outperforms the RNG model. Moreover, in contrast with the Reynolds stress and algebraic stress models, the RNG model requires lower computational time. Recently, the rather costly method of large eddy simulation (LES) has been of increasing interest amongst researchers. It is based on the approach of resolving large turbulent structures in space and time down to the grid limit everywhere in the flow. Large eddies are resolved directly, whereas small eddies are modelled (Van Balen *et al.* 2010). However, LES models require too much denser grids. The use of LES is very limited, and not efficient. Considering that the natural rivers are meandering in general, efficient overall investigations on meandering channel flow could have immediate practical importance on engineering application. In this case, it is not really needed to obtain all scales of secondary flow. Thus, we still need to rely on RANS (Reynolds-averaged Navier–Stokes) model (Stoesser *et al.* 2010). This is particularly true for mildly curved bend flows which have a small ratio of width B to the mean radius R, where the flow separation zone is negligible. RNG k–ϵ model can have effective predictive capabilities for secondary fluid motion in this state (Han *et al.* 2011).

In this paper, the study focuses on the simulation of secondary flow in a 180° meandering channel. Previous publications have been less involved in very detailed research in the special state, whose curvature ratio is $R/B = 3$, close to criticality. The details of flow pattern along the bend are studied. The variations of different components of velocity distribution, variations of secondary flow structures along the bend, contour of velocity along the bend, distribution of wall shear stresses and strength of secondary flow along the bend, are the major topics of this paper. Some important conclusions are drawn: secondary flow should be responsible for local asymmetry in the variations of velocity components; secondary flow takes effect starting from the inner bank; there exists empty space of maximum velocity in the downstream half bend; the strongest secondary flow occurs at about the 70° section, not the ideal 90° section; the variation tendency of bed shear stresses is similar to the velocities, etc.

INVESTIGATION METHODS

Experimental model

Experiments were carried out at the Institute for Sedimentation on River and Coastal Engineering, Tianjin University. The main channel is made up of a 180° bend with two straight inlet and outlet reaches. The rectangular cross-section is 0.3 m in height and 0.4 m in width. The radius of curvature of the inner bank and outer bank are 1.0 and 1.4 m, respectively. The lengths of straight inlet and outlet reaches are both 2.0 m. Figure 1 shows a schematic view of the channel and experimental set up. The bed and side walls of the channel are made of organic glass. Measurement of discharge was carried out by a calibrated flow meter set in the supply water pump. Experiments were conducted for an average discharge of 38.8 m^3/h. The water depth measured at the start of the channel was 0.15 m.

A three-dimensional downward facing acoustic Doppler velocity (ADV) meter was used to measure the three components of velocity, i.e. longitudinal, lateral and vertical components of velocity. They were measured at 12 non-uniform levels of water depth and at seven lateral distances along the channel width. The lateral spacing distance of the measuring line was 5 cm. The measurements were performed at sections with intervals of 30° along the bend.

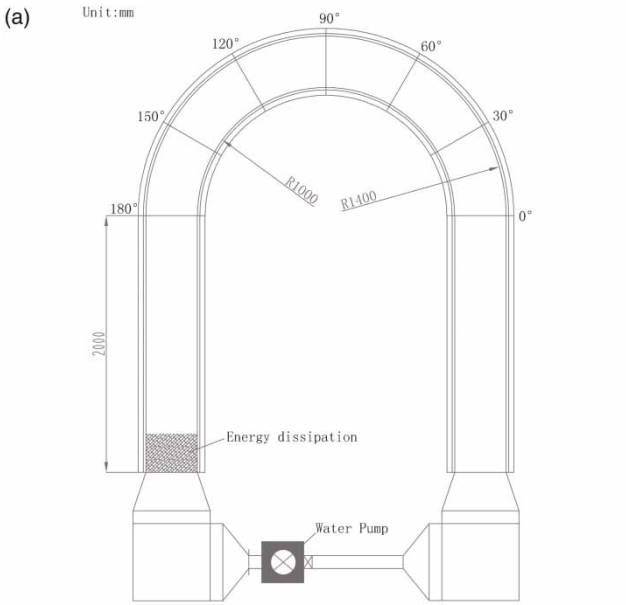

Figure 1 | (a) Schematic view of 180° channel and (b) picture of experimental set up.

Figure 2 shows the grid points used for the velocity measurement at each cross-section in the bend.

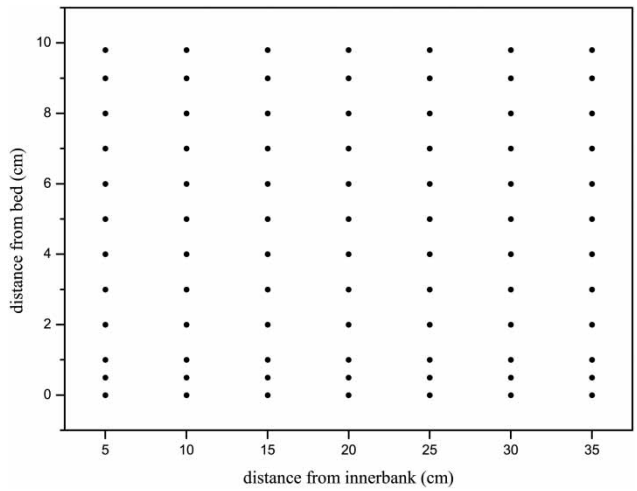

Figure 2 | Grid points for velocity measurement.

Numerical model

Mathematical model

In the RNG k–ϵ model, the effect of small-scale turbulence is represented through a random forcing function in the Navier–Stokes equations. The RNG model systematically removes all small scales of motion from the governing equations by considering their effects in terms of larger scale motion and a modified viscosity. This model was derived using a rigorous statistical technique. The main governing equations are as follows.

Continuity equation:

$$\frac{\partial \bar{u}_i}{\partial x_i} = 0 \tag{1}$$

Momentum equation:

$$\frac{\partial \bar{u}_i}{\partial t} + \frac{\partial \bar{u}_i \bar{u}_j}{\partial x_j} = -\frac{1}{\rho}\frac{\partial \bar{p}}{\partial x_i} + \frac{\partial}{\partial x_j}\left(\nu \frac{\partial \bar{u}_i}{\partial x_j} - \overline{u_i' u_j'}\right) \tag{2}$$

$k-\varepsilon$ equation:

$$\frac{\partial k}{\partial t} + \bar{u}_i \frac{\partial k}{\partial x_i} = \frac{\partial}{\partial x_i}\left[\left(\nu + \frac{\nu_t}{\sigma_k}\right)\frac{\partial k}{\partial x_i}\right] - \overline{u_i' u_j'}\frac{\partial \bar{u}_i}{\partial x_j} - \varepsilon \tag{3}$$

$$\frac{\partial \varepsilon}{\partial t} + \bar{u}_i \frac{\partial \varepsilon}{\partial x_i} = -\frac{\partial}{\partial x_i}\left[\left(\nu + \frac{\nu_t}{\sigma_\varepsilon}\right)\frac{\partial \varepsilon}{\partial x_i}\right] - c_1 \frac{\varepsilon}{k}\overline{u_i' u_j'}\frac{\partial \bar{u}_i}{\partial x_j} - c_2 \frac{\varepsilon^2}{k} \tag{4}$$

where ρ is the density of the fluid, $\bar{u}$ is the temporal average velocity, $\bar{p}$ is the pressure, ν is the kinematic viscosity, k and ε are the turbulent kinetic energy and the dissipation rate, respectively.

$-\overline{u_i'u_j'}$ stands for the Reynolds stress tensor

$$-\overline{u_i'u_j'} = \nu_t\left(\frac{\partial \bar{u}_i}{\partial x_j}+\frac{\partial \bar{u}_j}{\partial x_i}\right)-\frac{2}{3}k\delta_{ij};$$

$$-\overline{u_i'u_j'}\frac{\partial \bar{u}_i}{\partial x_j}$$

represents the generation of turbulence kinetic energy due to the mean velocity gradients

$$\nu_t = \frac{c_\mu k^2}{\varepsilon}$$

represents the kinematic eddy viscosity.

It is worth noting that all the values of the constants (except β) are derived explicitly in the RNG procedure. They are given below with the commonly used values

$$c_\mu = 0.0845 \cdot c_1 = 1.42, \quad c_2 = 1.68 + \frac{c_\mu \eta^3\left(1-\frac{\eta}{\eta_0}\right)}{1+\beta\eta^3} \tag{5}$$

where $\eta = \frac{|S|k}{\varepsilon}$, $\eta_0 = 4.38$, $\beta = 0.012$ (derived from experiment).

The turbulent Prandtl numbers for k and ε are: $\sigma_k = \sigma_\varepsilon = 0.7194$.

The modulus of the mean rate-of-strain tensor is

$$|S| \equiv \sqrt{2\bar{S}_{ij}\bar{S}_{ij}} \tag{6}$$

where the mean strain rate is

$$\bar{S}_{ij} = \frac{1}{2}\left(\frac{\partial \bar{u}_i}{\partial x_j}+\frac{\partial \bar{u}_j}{\partial x_i}\right).$$

Calculation method

The calculation domain is the same as the experimental domain. The structured and non-uniform grids are used, as shown in Figure 3. The free surface is treated as a plane of symmetry where zero-gradient conditions are applied for the variables parallel to the surface with the wall-normal variables set to zero. For rather small Froude numbers, this treatment is considered accurate enough as water level variations were reported very small (less than 5% of the water depth) in the experiment (Stoesser *et al.* 2010). The velocity inlet condition is imposed on the inflow boundary, and the outflow outlet condition is imposed on the outlet boundary. The no-slip boundary condition is used at the bed and the side walls. A finite volume method is used to discretize and solve the governing equations. The pressure-based coupled algorithm is used for the pressure-velocity coupling at each iteration step. The momentum equations are discretized using the Second Order Upwind scheme, for obtaining the face fluxes for all cells. The PRESTO! Scheme is used for pressure interpolation, and the turbulence model equations are also second order accurate.

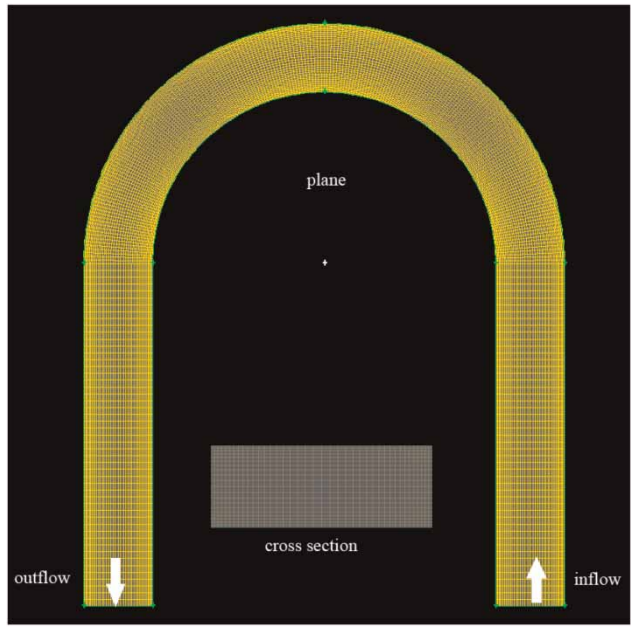

Figure 3 | Schematic view of grids used in the numerical model.

RESULTS AND DISCUSSION

Longitudinal velocity distribution

When flow approaches the bend, the secondary flow is generated gradually and causes changes in the velocity components at three directions, x, y, and z. Due to the presence of secondary flow in the bend, the maximum value of the longitudinal velocity occurs below the water

surface and is average at the mid-depth of flow. Mainly, the distribution of longitudinal velocity is not logarithmic in the channel bend. Figures 4(a)–(g) show typical comparisons of RNG k–ϵ simulated and experimental values of longitudinal velocity distributions at seven sections along the bend, i.e. at sections 0, 30, 60, 90, 120, 150 and 180°, respectively. Moreover, it can intuitively show the location of maximum longitudinal velocity at each measuring line.

It is seen that the RNG numerical simulation is in reasonable agreement with the experimental measurements. The average R^2 estimates for each section are 0.865, 0.839, 0.916, 0.925, 0.907, 0.933, and 0.921. However, some obvious deviations between numerical and experimental results are found in some regions of the meandering channel, especially in Figures 4(a) and (b). This is because there distortion and imbalance exists in the junction of the curved part and inflow straight part. It is caused in the

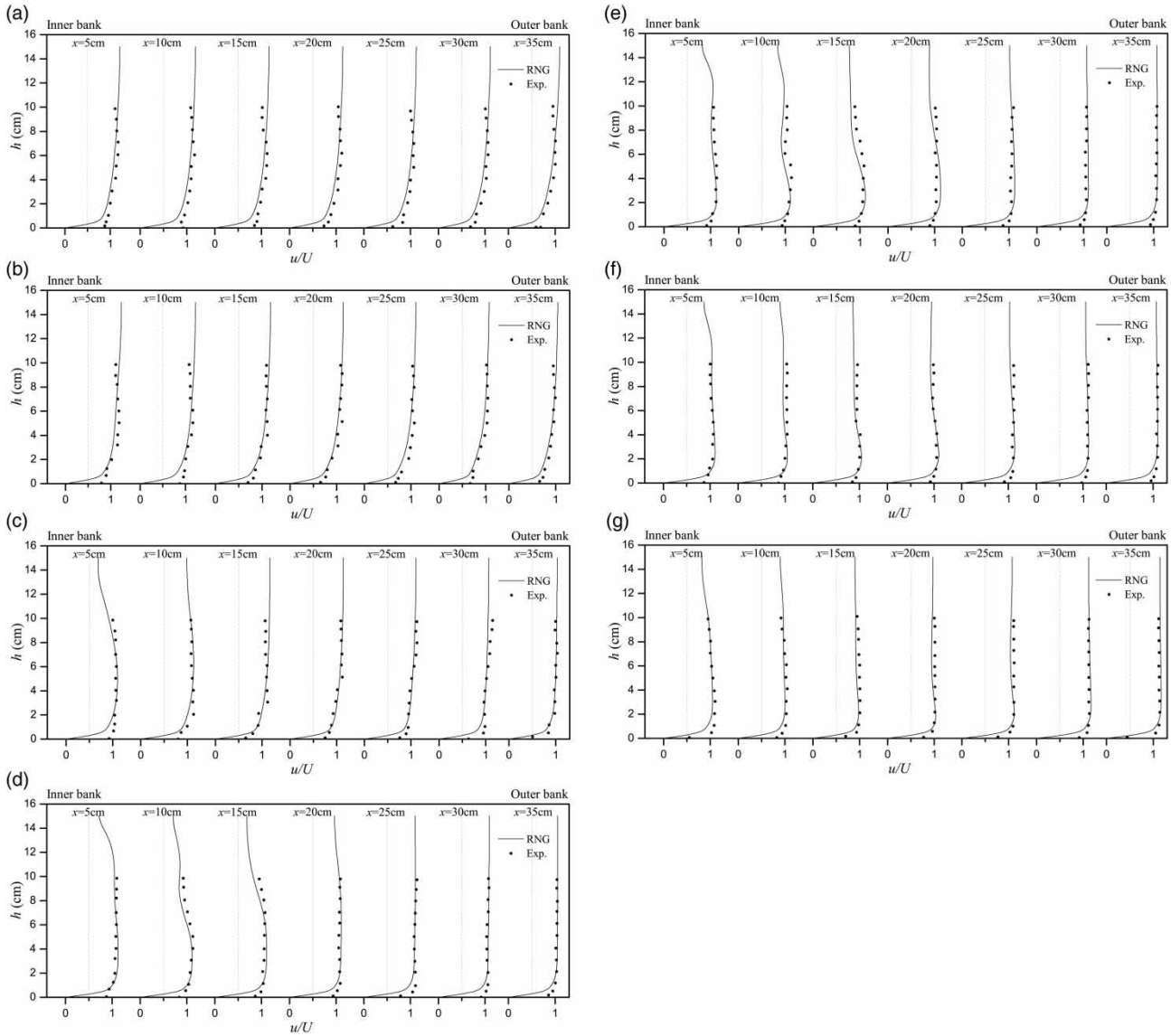

Figure 4 | Longitudinal velocity distributions at sections: (a) 0°, (b) 30°, (c) 60°, (d) 90°, (e) 120°, (f) 150° and (g) 180° (x: the distance from inner bank; U: the average velocity of cross-section).

flume assembling process. The similar deviations below (i.e. Figures 5 and 6) are also for the same reason.

Figures 4(a) and (b) show that the maximum values of longitudinal velocity occur near the water surface. At these sections, the influence of the secondary flow is not significant. Figure 4(c) shows that the influence of the secondary flow on the primary flow becomes considerable. As a result, starting from section 60° of the bend, the location of maximum longitudinal velocity from near the inner bank moves towards the outer bank and, from the water surface, moves towards the bed simultaneously. In the downstream half bend, the influence of secondary flow has been very strong, the changes of longitudinal velocity are very obvious. In the end, the locations of maximum longitudinal velocity are just about 2 cm from the bed, as shown in Figure 4(g). Generally, Figure 4 shows that changes in longitudinal velocity near the inner bank are more dramatic

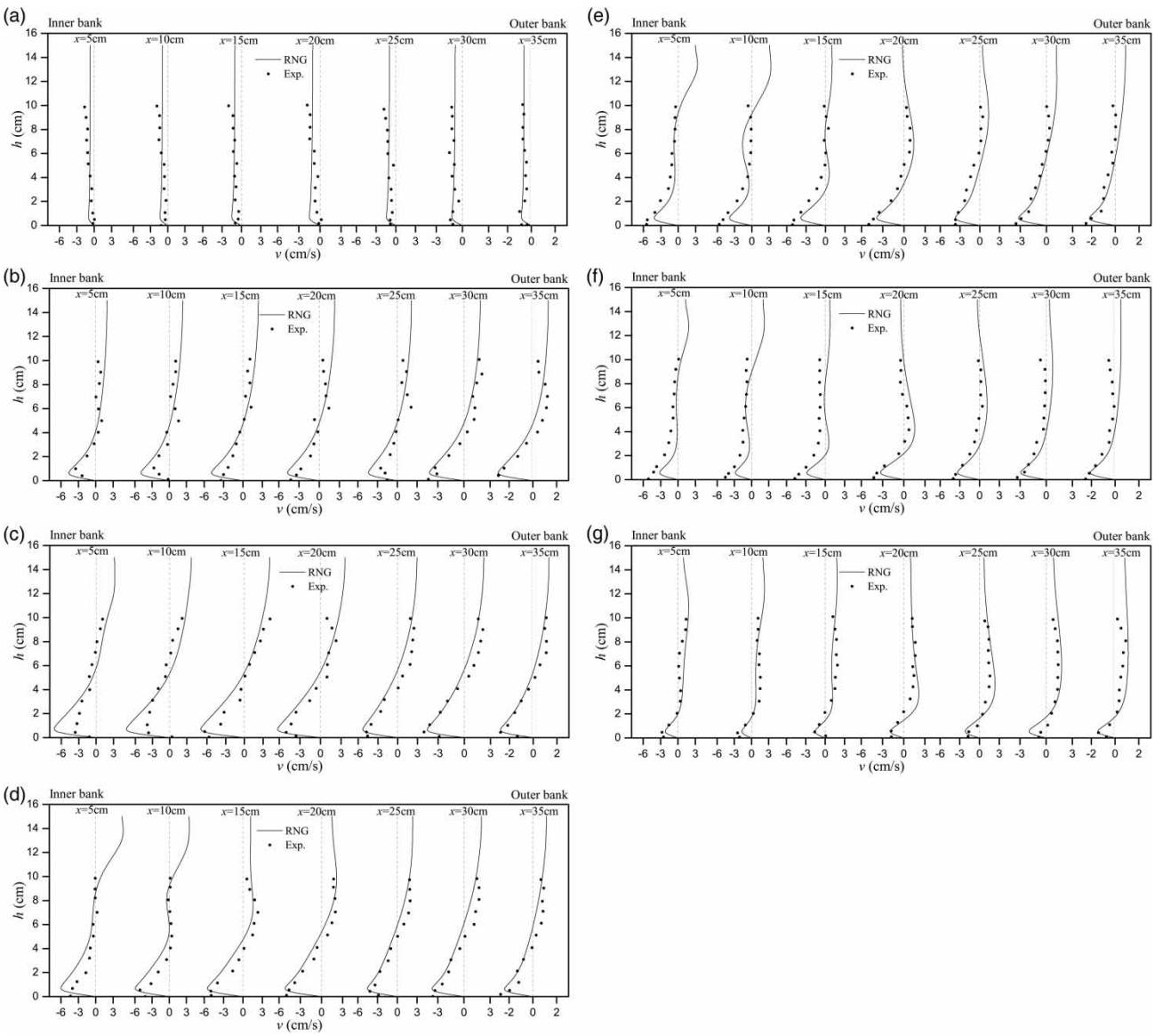

Figure 5 | Lateral velocity distribution at sections: (a) 0°, (b) 30°, (c) 60°, (d) 90°, (e) 120°, (f) 150° and (g) 180°.

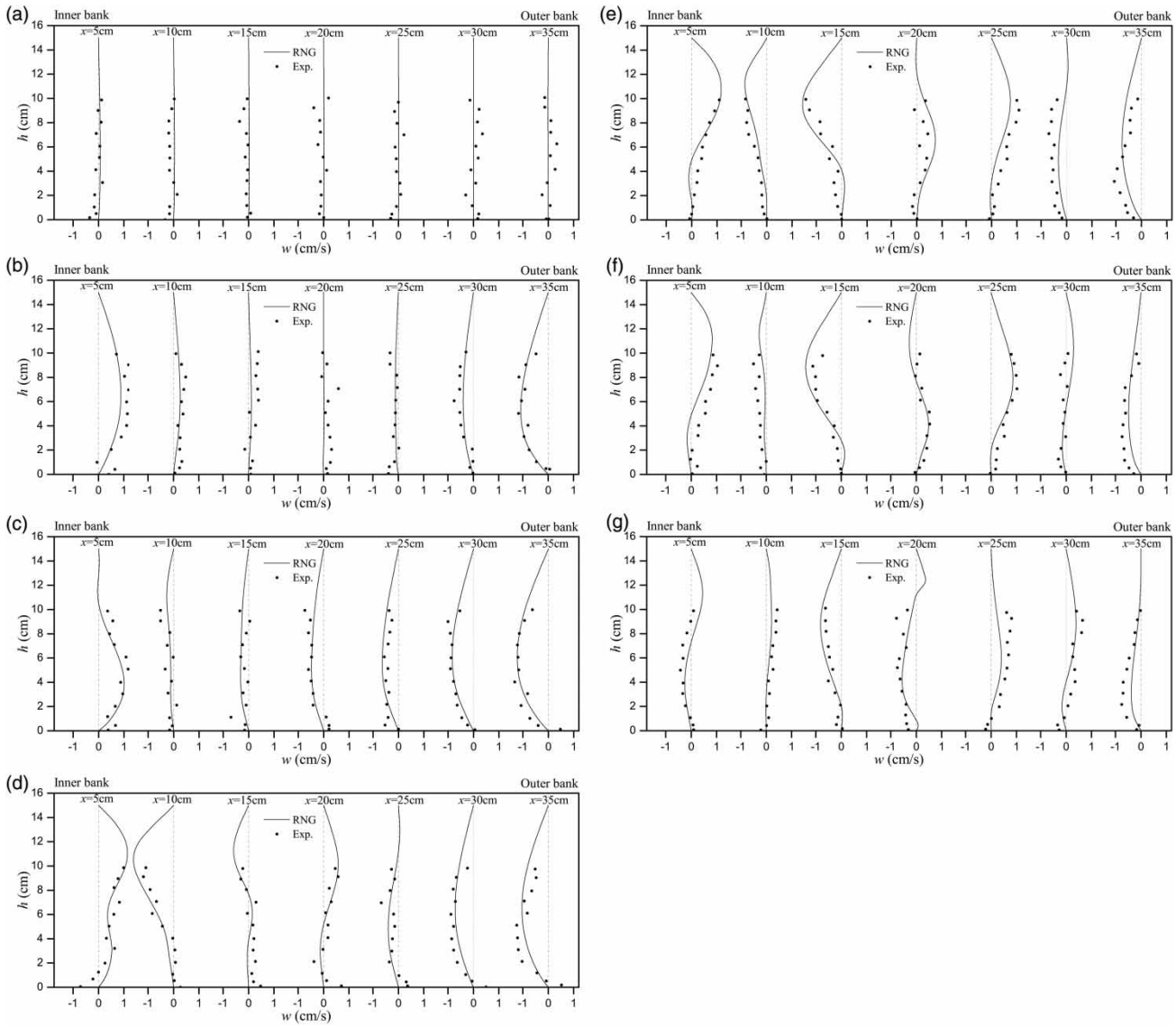

Figure 6 | Vertical velocity distribution at sections: (a) 0°, (b) 30°, (c) 60°, (d) 90°, (e) 120°, (f) 150° and (g) 180°.

compared with the outer bank, secondary flow takes effect starting from the inner bank. Ye & McCorquodale (1998), Jing *et al*. (2009) and Abhari *et al*. (2010) reported similar results in a 90, 180 and 270° channel bend. They showed that secondary flow is responsible for local variations in velocity components. Moreover, in all sections, there are some deviations between numerical and measured data near the bed. The possible reason may be that the flow conditions near the bed are incredibly complex and the flume bed is not exactly horizontal. Enhanced wall treatment (Zhang *et al*. 2007) may need to be added to the numerical model in the future, as it could provide the most consistent wall shear stress predictions with the least sensitivity to y^+ values. It automatically blends all solution variables from their viscous sublayer formulation to the corresponding logarithmic layer values depending on y^+. Our employed standard wall function did not have this ability.

Lateral velocity distribution

In a meandering channel, the centrifugal force increases the water level near the outer bank and decreases the water level near the inner bank. As a result, under the effect of pressure gradient, flow is directed toward the inner bank near the bed and toward the outer bank near the water surface. Figure 5 shows typical comparisons of RNG simulated and experimental values of lateral velocity distribution at seven sections. The predictions in the bend agree well with the experimental data. From the 120–180° section, the numerical value is slightly greater than the measured data. This may be a common problem of the RANS model. Stoesser *et al.* (2010) indicated that the RANS code, no matter what turbulence model employed, overpredicts the scale and strength of the outer-bank secondary cell, due to the employed isotropic turbulence models in RANS. Generally, the positive values of lateral velocity near the water surface and the negative values near the bed confirm the presence of secondary flow in the channel bend.

Figures 5(a)–(c) show that due to weak secondary flow, the variations in lateral velocity are almost the same at each measuring line of the respective section. Then, starting from sections 60° of the bend, the lateral distribution shapes change gradually. At the 90° section, the distribution shape shows large fluctuations near the inner bank, and the locations of maximum positive value of lateral velocity near the mid channel from the water surface move towards the bed. This changes effects from near the inner bank spreading towards the outer bank. At the end of the channel, the distribution shape fluctuations disappear in the domain between inner bank and mid-channel, while the maximum positive value of lateral velocity has been located below the mid-depth of flow in the domain between the mid-channel and outer bank.

Moreover, it was found that the magnitude of lateral velocity is almost 15–35% of longitudinal velocity. The variation tendency of lateral velocity is more complex than longitudinal velocity, though both have some similarities. The reason may be that the secondary flow has a greater effect on lateral velocity.

Vertical velocity distribution

In a channel bend, the values of velocity at three directions are important because the interaction of the primary flow and the secondary flow leads to a complex three-dimensional helical flow. Figure 6 shows typical comparisons of numerical and experimental values of vertical velocity at seven different sections. It is obviously seen that the maximum values of vertical velocity at the 30° section occurs near the inner bank and the outer bank. However, the value of vertical velocity is positive near the inner bank and negative near the outer bank. Their distribution shape is convex to the opposite bank, and this shape 'influence' spreads towards the opposite bank further downstream, gradually along the bend.

At the 60° section, the 'influence' of the outer bank has reached the inner bank, as shown in Figure 6(c). The value of vertical velocity is almost negative except for the zone near the inner bank. Though there is some delay, the 'influence' of the inner bank reaches the mid-channel at section 90°, as shown in Figure 6(d). The distribution shapes near the inner bank appear to fluctuate due to the interaction of two directional 'influences'. Then, starting from this section, the variation tendencies of vertical velocity at each measuring line are significantly semblable, as shown in Figures 6(d)–(g). That is, fluctuations seem to be weaker and weaker, and the distribution shapes at each measuring line all get much closer to the straight line. At the end of the bend, two directional 'influences' both reach the opposite bank. However, they almost disappear.

Additionally, Figure 6 shows that the values of vertical velocity at the centreline of the channel are negligible. Generally, the magnitude of vertical velocity is almost 5–10% of the longitudinal velocity.

It is evident from Figures 4–6 that the RNG k–ϵ model is capable of simulating the flow along the bend, both accurately and efficiently.

Velocity horizontal distribution along the bend

The special feature of flow in the bend leads to a complex pressure gradient between the inner bank and outer bank. The comparison of calculated velocity distribution along the bend at different horizontal planes is shown in Figure 7. Generally, at the start of the bend, due to the negative pressure gradient at the inner bank, the location of maximum velocity is near the inner bank, however, by further downstream in the bend, as the secondary flow grows, the

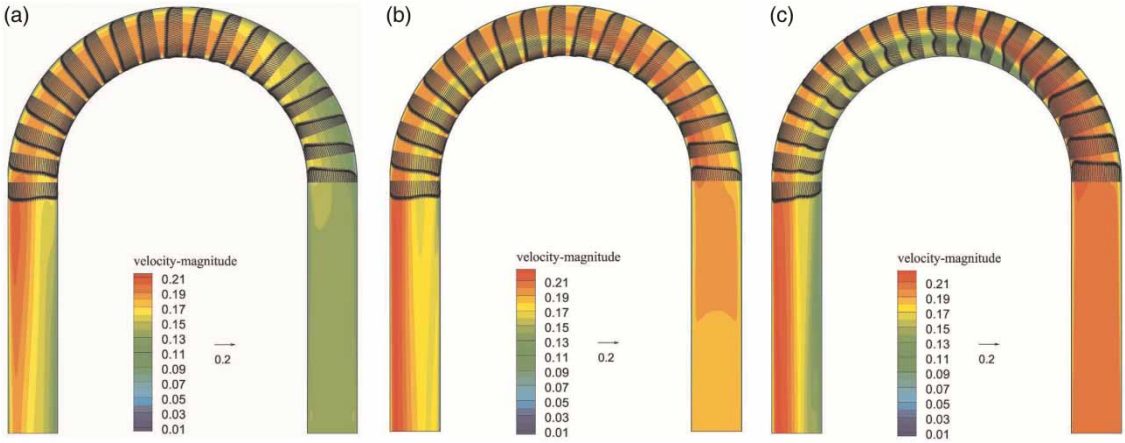

Figure 7 | Calculated velocity distribution and contour at different horizontal planes: (a) near the bed, (b) mid depth of flow, (c) near the surface.

location of maximum velocity shifts to the mid channel and ultimately to the outer bank at the end of the bend. However, there exists an empty space of maximum velocity in the downstream half bend.

Moreover, according to the comparison of Figures 7(a)–(c), it is evident that near the bend and the mid depth of flow, the streamlines deflect toward the inner bank. However, near the water surface, the streamlines deflect toward the outer bank, as shown in Figure 7(c). This demonstrates that due to the presence of secondary flow in the bend, with an increase of distance from the bed level, the streamlines deflect from the inner bank to the outer bank. It is not obvious below the mid depth of flow, but there exist complex changes near the water surface.

Secondary flow structures

The secondary flow is one of the prominent features of flow in a channel bend. As a result of imbalance between the lateral water surface pressure gradient and centrifugal force, the secondary flow forms in the bend. The centrifugal force near the water surface prevails over the inward pressure gradient, resulting in an outward flow near the water surface and an inward flow near the bed. The circulation pattern along the bend is shown in Figure 8. Figures 8(a)–(c) show that by moving to the downstream, the vortex core moves closer to the inner bank. However, when it reaches the apex of the bend, i.e. the 90° section, the vortex core moves upward, and another new vortex forms in the mid channel. Two clockwise circulations appear in the bend as shown in Figure 8(d). Figures 8(d)–(f) show that after the apex of the bend, the two vortex cores moves closer to the outer bank. Due to interaction of the two vortexes, a small anticlockwise circulation is generated in the upper zone of the mid channel. It does not survive for very long and disappears at the end of the channel, as shown in Figure 8(g). Meanwhile, the main two vortex cores have been moving toward the bed and also nearly disappear in the exit.

The calculated contours of longitudinal velocity at different sections along the bend are also depicted in Figure 8. Figure 8(a) shows that at the start of the bend the zone of maximum longitudinal velocity is near the inner bank and water surface. However, when the secondary flow forms in the bend, this causes the lateral momentum transfer toward the outer bank (Figures 8(a)–(c)), the 'maximum' zone shrink in the lateral direction and its core also seems to be moving towards the outer bank. This in turn shows that the centrifugal force generates secondary flow which results in the three-dimensional helicoidally flow pattern and, subsequently, this influences the flow behaviour and lateral momentum transport. It is worth noting that the 'maximum' zone moves in the direction opposite to the vortex core. Figures 8(d)–(f) show that as two vortexes emerge, the 'maximum' zone separates into two parts. The larger one follows the new vortex, the smaller one follows the old one, and they both approach the bed, but the smaller one gets smaller and smaller as

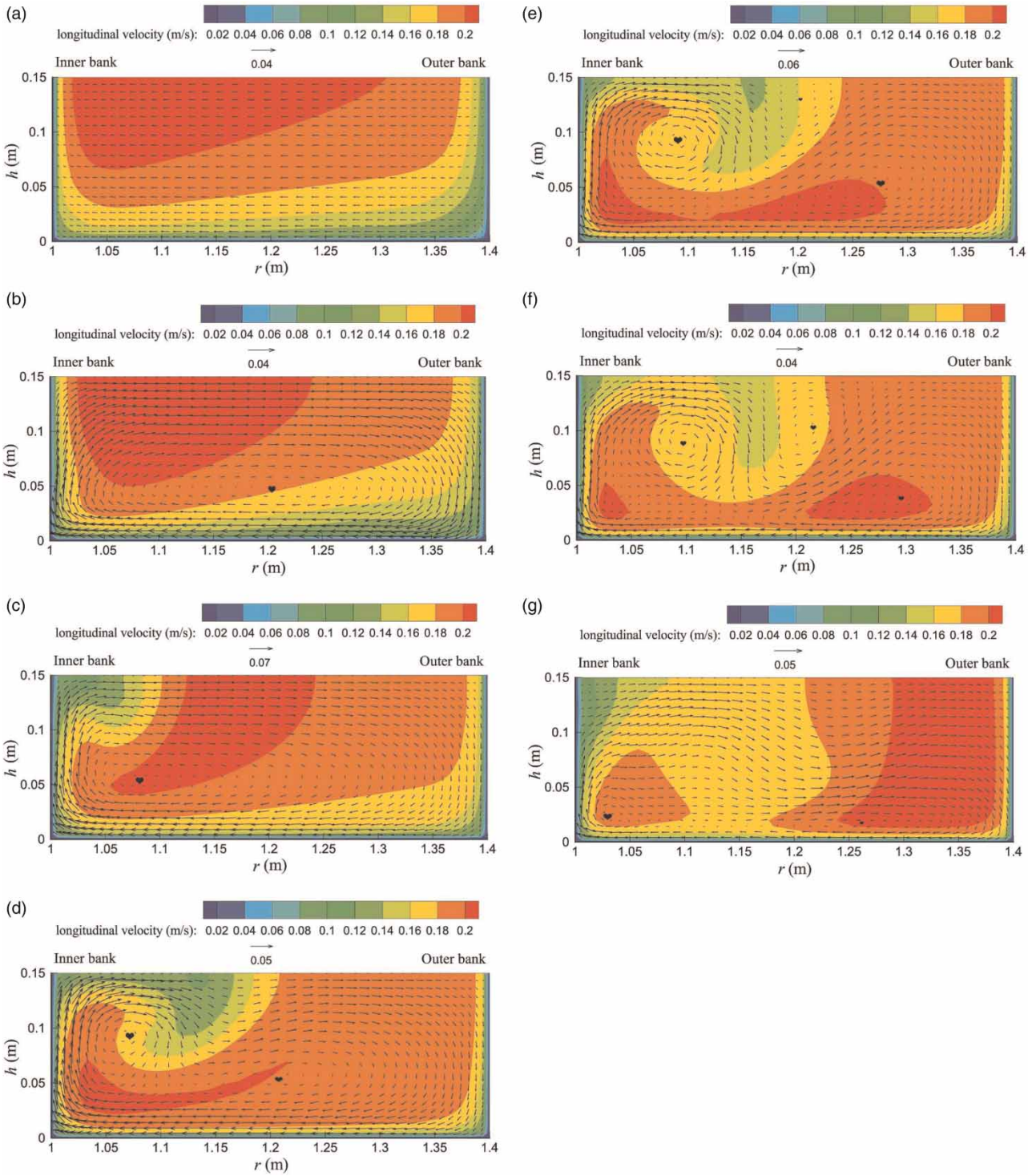

Figure 8 | Calculated streamlines of secondary flow and contours of longitudinal velocity at sections: (a) 0°, (b) 30°, (c) 60°, (d) 90°, (e) 120°, (f) 150° and (g) 180° (*r*: radial coordinate).

the two vortexes move closer to the outer bank. In the exit section, as two main vortexes retract inward and approximately disappear towards the bed, the 'maximum' zone returns to its original scale and arrives at the outer bank, as shown in Figure 8(g). It is evident that the centrifugal force dominates near the water surface; the inward pressure gradient dominates near the bed; the primary flow and secondary flow influence each other.

The above analyses help for the prediction of erosion and deposition zone, in the case of a movable bed. If the bed is movable, sediment will deflect from the outer bank to the inner bank. Therefore, we can expect erosion near the outer bank and deposition near the inner bank in a movable bed channel.

Wall shear stresses

The wall shear stresses play an important role in the process of sediment transport. The knowledge of wall shear stresses helps to estimate the zones of bed-load transportation, erosion and deposition of sediment in bend channels. The wall shear stress τ, was estimated by using the wall laws (Olsen 2006)

$$\tau = \rho(U^+)^2 \tag{7}$$

where

$$U^+ = \frac{\kappa U}{\ln\left(\frac{30y}{k_s}\right)} \tag{8}$$

where U is the velocity, U^+ is the shear velocity, y is the distance from the wall and k_s is the wall roughness. The values of wall shear stresses were calculated by using Equation (7) and are plotted in Figure 9. The distribution of sidewall shear stresses and contour of bed wall shear stresses along the bend are shown in Figures 9(a) and (b), respectively.

It can be clearly seen that at the start of the bend the outer bank shear stresses are smaller than the inner ones, the maximum bed wall shear stresses is located near the inner bank. When the secondary flow grows in the bend, the zone of maximum bed shear stresses deflects gradually

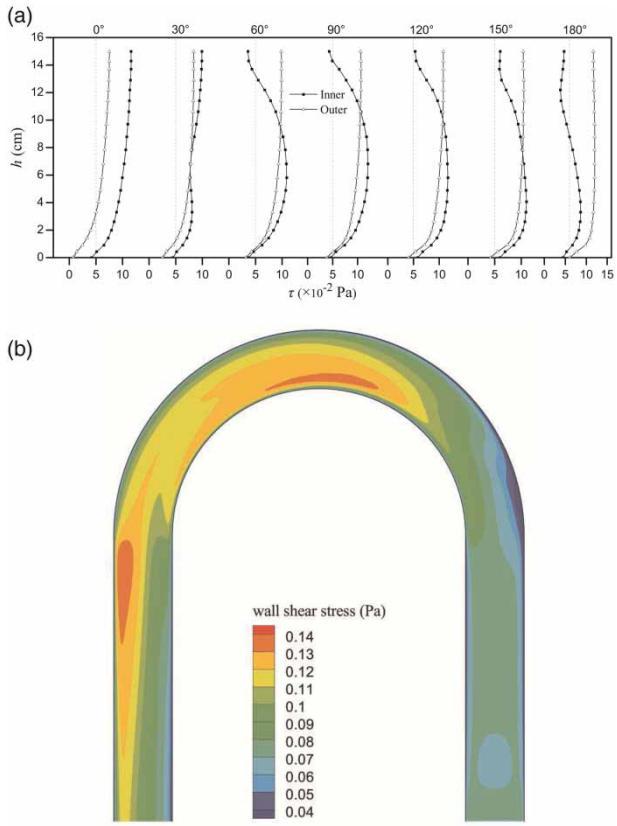

Figure 9 | Calculated distribution of wall shear stresses along the bend: (a) sidewall and (b) bed.

toward the outer bank. In the process, the magnitude of inner and outer bank shear stresses is very similar. While starting from section 30°, the outer bank shear stresses are larger above the two-thirds of water depth from the bed; the inner ones are larger below this depth. Moreover, the inner bank shear stresses can reach a local minimum both at the bed and the water surface. At the end of the bend, the zone of maximum bed shear stresses is close to the outer bank, whose shear stresses are much larger than the inner bank. It is worth noting that the variation tendency of the wall shear stresses is similar to the stream-wise velocity distribution. This is in accordance with the simulated results of Van Balen *et al.* (2009).

Strength of secondary flow

In this paper, the strength of secondary flow at each section is taken as the integral for helicity on a specific section. Helicity is the extent to which helix-like motion occurs, defined

by the dot product of vorticity and the velocity vector ($\boldsymbol{V}$)

$$H = (\nabla \times V) \cdot V \tag{9}$$

The strength of secondary flow I is given by (Berger & Field 1984)

$$I = \int_V H \mathrm{d}^3 x \tag{10}$$

The strength of secondary flow for different approach Reynolds numbers Re was computed by Equation (10) and is depicted in Figure 10. This figure shows that the strength of secondary flow for all Reynolds numbers increases sharply up to the 70° section. After this section, the strength of secondary flow decreases slightly and reaches a relatively small value in the end. The strongest secondary flow occurs at upstream of the apex, at about the 70° section, not the ideal 90° section. This is consistent with the experimental results of Shukry (1950), which show that the maximum transverse slope of water surface, as the comprehensive reflection of strength of secondary flow, occurs at about the 70° section. Moreover, the strength of the 180° section is stronger than the 0° section, which illustrates that secondary flow does not disappear immediately at the end of the bend, it needs a longer straight outlet reach to die out (Zhang & Lv 1993), as in the experimental flume of Li *et al.* (2013).

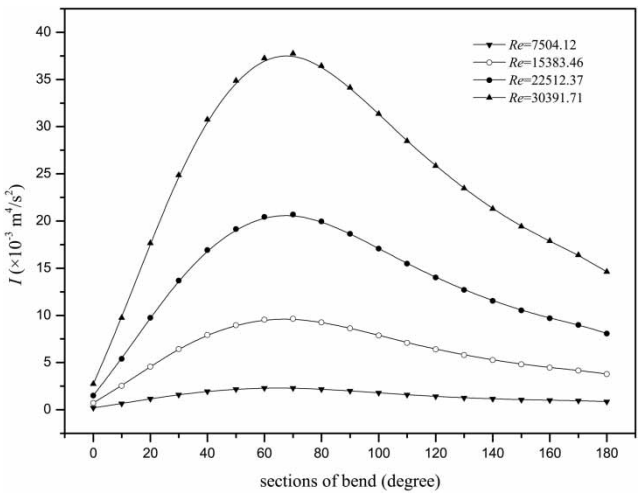

Figure 10 | Calculated strength of secondary flow along the bend.

CONCLUSIONS

The RNG k–ϵ numerical model together with Micro ADV are adopted to investigate the mildly curved 180° open-channel flow. The main conclusions are as follows:

(1) The variations of longitudinal, lateral and vertical velocity components were analyzed numerically and experimentally. The investigation shows that secondary flow in a channel bend is responsible for local asymmetry in the variations of velocity components.
(2) There exist complex secondary flow structures in the bend. Numerical simulation and experimental data indicate the effective zone of secondary flow in the channel bend, that is, about the 60–180° section. The location of maximum longitudinal velocity is near the water surface, up to about the 30° section; as flow progresses further downstream, it not only moves from the water surface towards the bed, but from the inner bank moves towards the outer bank simultaneously. Secondary flow takes effect starting from the inner bank, and the variations of longitudinal velocity near the inner bank are more severe.
(3) Secondary flow causes the lateral momentum transportation towards the outer bank and interferes in logarithmic longitudinal velocity distribution. It imposes a stronger effect on lateral velocity and vertical velocity, resulting in their more complex variations than longitudinal velocity.
(4) The streamlines deflect towards the inner bank away from the water surface; on the contrary, it deflects towards the outer bank near the water surface. Maximum velocity has a similar variation tendency, and its sharp deflection towards the outer bank occurs at the section where the secondary flow has maximum strength, i.e. the 70° section. It needs to pass through an empty space of maximum velocity in the downstream half bend and reach to the outer bank in the exit.
(5) The centrifugal force dominates near the water surface, the inward pressure gradient dominates near the bed, and their interaction results in complex secondary flow structures. Primary flow and secondary flow influence each other, rendered in the mutual change of longitudinal velocity and secondary flow structures at cross-sections.

(6) The variation tendency of bed shear stresses is similar to the velocities. At the start of the bend, the maximum bed shear stress is located near the inner bank. In the end, the zone of maximum shear stresses is close to the outer bank. Meanwhile, for side-wall shear stresses, at first the outer bank shear stresses are smaller than the inner ones, then they ultimately outdistance the opposite side.
(7) The strength of secondary flow increases up to about the 70° section, reaching a maximum value and thereafter decreasing. The increasing approach Reynolds number is associated with increasing the strength of secondary flow.
(8) The RNG k–ϵ numerical model used in this study could efficiently simulate the flow pattern in a mild 180° bend.

However, despite the encouraging results, there still exist some limitations in the study. The experimental model is not perfect: the flume bed is not exactly horizontal and the flow discharge is difficult to maintain a constant. Thus, experimental data is inevitably slightly different from the true value. Better manufacturing and installation techniques for the flume and a more stable water pump are really needed for improving experimental work. In addition, the RNG k–ϵ model is selected through the comparisons among the existing developed models. Any model has its advantages and disadvantages. The RNG k–ϵ model is quite efficient but certainly not the best. A new model that could overcome the limitations of RANS models and adopt the advantages of LES model perhaps would improve efficient investigation ability much more. That could be the focus of future research.

ACKNOWLEDGEMENT

This research was supported by the National Natural Science Foundation of China, Grant Nos 51279124, 51021004 and 50979066.

REFERENCES

Abad, J. D. & Garcia, M. H. 2009 Experiments in a high amplitude Kinoshita meandering channel: 1. Implications of bend orientation on mean and turbulent flow structure. *Water Resour. Res.* **45** (2), W02401.

Abhari, M. N., Ghodsian, M., Vaghefi, M. & Panahpur, N. 2010 Experimental and numerical simulation of flow in a 90° bend. *Flow Meas. Instrument.* **21** (3), 292–298.

Berger, M. A. & Field, G. B. 1984 The topological properties of magnetic helicity. *J. Fluid Mech.* **147**, 133–148.

Blanckaert, K. & Graf, W. H. 2001 Mean flow and turbulence in open-channel bend. *J. Hydraul. Eng.* **127** (10), 835–847.

Blanckaert, K. & de Vriend, H. J. 2003 Nonlinear modeling of mean flow redistribution in curved open channels. *Water Resour. Res.* **39** (12), 1375.

Blanckaert, K. & Graf, W. H. 2004a Momentum transport in sharp open-channel bends. *J. Hydraul. Eng.* **130** (3), 186–198.

Blanckaert, K. & de Vriend, H. 2004b Secondary flow in sharp open-channel bends. *J. Fluid Mech.* **498** (1), 353–380.

Chen, W. & Chau, K. 2006 Intelligent manipulation and calibration of parameters for hydrological models. *Int. J. Environ. Pollut.* **28** (3), 432–447.

Cheng, C., Chau, K., Sun, Y. & Lin, J. 2005 *Long-term prediction of discharges in Manwan Reservoir using artificial neural network models, Advances in Neural Networks – ISNN 2005*. Springer, Germany, pp. 1040–1045.

Chau, K., Wu, C. & Li, Y. 2005 Comparison of several flood forecasting models in Yangtze River. *J. Hydrol. Eng.* **10** (6), 485–491.

Einstein, H. & Harder, J. 1954 Velocity distribution and the boundary layer at channel bends. *Trans. Am. Geophys. Union* **35** (1), 114–120.

Fischer-Antze, T., Rüther, N., Olsen, N. R. & Gutknecht, D. 2009 Three-dimensional (3D) modelling of non-uniform sediment transport in a channel bend with unsteady flow. *J. Hydraul. Res.* **47** (5), 670–675.

Han, S. S., Biron, P. M. & Ramamurthy, A. S. 2011 Three-dimensional modelling of flow in sharp open-channel bends with vanes. *J. Hydraul. Res.* **49** (1), 64–72.

Jing, H., Guo, Y., Li, C. & Zhang, J. 2009 Three-dimensional numerical simulation of compound meandering open channel flow by the Reynolds stress model. *Int. J. Numer. Method. Fluids* **59** (8), 927–943.

Keevil, G. M., Peakall, J., Best, J. L. & Amos, K. J. 2006 Flow structure in sinuous submarine channels: Velocity and turbulence structure of an experimental submarine channel. *Mar. Geol.* **229** (3), 241–257.

Kikkawa, H., Ikeda, S., Ohkawa, H. & Kawamura, Y. 1973 Secondary flow in a bend of turbulent stream. *Proceedings of Japan Society of Civil Engineers*, Japan, pp. 107–114.

Launder, B. E. & Spalding, D. 1974 The numerical computation of turbulent flows. *Comput. Method. Appl. Mech. Eng.* **3** (2), 269–289.

Li, Q., Song, J. F., Li, C., Wei, Y. D. & Chen, J. Y. 2013 Numerical and experimental study of particle deposition on inner wall of 180° bend. *Powder Technol.* **237**, 241–254.

Muttil, N. & Chau, K.-W. 2006 Neural network and genetic programming for modelling coastal algal blooms. *Int. J. Environ. Pollut.* **28** (3), 223–238.

Olsen, N. R. B. 2003 Three-dimensional CFD modeling of self-forming meandering channel. *J. Hydraul. Eng.* **129** (5), 366–372.

Olsen, N. R. B. 2006 *A Three-Dimensional Numerical Model for Simulation of Sediment Movements in Water Intakes with Multiblock Option. User's Manual*. The Norwegian University of Science and Technology, Trondheim.

Ouillon, S. & Dartus, D. 1997 Three-dimensional computation of flow around groyne. *J. Hydraul. Eng.* **123** (11), 962–970.

Ramamurthy, A., Han, S. & Biron, P. 2012 Three-dimensional simulation parameters for 90° open channel bend flows. *J. Comput. Civil Eng.* **27** (3), 282–291.

Shukry, A. 1950 Flow around bends in an open flume. *Am. Soc. Civ. Eng.* **115** (1), 751–779.

Soliman, M. M. & Tinney, E. 1968 Flow around 180 degree bends in open rectangular channels. *J. Hydraul. Div.* **94** (4), 893–908.

Stoesser, T., Ruether, N. & Olsen, N. R. B. 2010 Calculation of primary and secondary flow and boundary shear stresses in a meandering channel. *Adv. Water Res.* **33** (2), 158–170.

Sudo, K., Sumida, M. & Hibara, H. 1998 Experimental investigation on turbulent flow in a circular-sectioned 90-degree bend. *Exp. Fluids.* **25** (1), 42–49.

Taormina, R., Chau, K.-W. & Sethi, R. 2012 Artificial neural network simulation of hourly groundwater levels in a coastal aquifer system of the Venice lagoon. *Eng. Appl. Artif. Intel.* **25** (8), 1670–1676.

Termini, D. & Piraino, M. 2011 Experimental analysis of cross-sectional flow motion in a large amplitude meandering bend. *Earth Surf. Proc. Land.* **36** (2), 244–256.

Thorne, C. R., Zevenbergen, L., Pitlick, J., Rais, S., Bradley, J. & Julien, P. 1985 Direct measurements of secondary currents in a meandering sand-bed river. *Lett. Nat.* **315** (27), 746–747.

Van Balen, W., Uijttewaal, W. & Blanckaert, K. 2009 Large-eddy simulation of a mildly curved open-channel flow. *J. Fluid Mech.* **630** (1), 413–442.

Van Balen, W., Blanckaert, K. & Uijttewaal, W. 2010 Analysis of the role of turbulence in curved open-channel flow at different water depths by means of experiments, LES and RANS. *J. Turbul.* **11** (12), 1–30.

Wormleaton, P. R. & Ewunetu, M. 2006 Three-dimensional k–ϵ numerical modelling of overbank flow in a mobile bed meandering channel with floodplains of different depth, roughness and planform. *J. Hydraul. Res.* **44** (1), 18–32.

Wilson, C., Guymer, I., Boxall, J. & Olsen, N. 2007 Three-dimensional numerical simulation of solute transport in a meandering self-formed river channel. *J. Hydraul. Res.* **45** (5), 610–616.

Wu, C., Chau, K. & Li, Y. 2009 Predicting monthly streamflow using data-driven models coupled with data-preprocessing techniques. *Water Resour. Res.* **45** (8), W08432, DOI: 10.1029/2007WR006737

Xu, D., Liu, Z., Qian, A. & Bai, Y. 2010 Three-dimensional numerical simulation of flow in river bends. *J. Hydraul. Eng.* **41** (12), 1423–1431 (in Chinese).

Ye, J. & McCorquodale, J. 1998 Simulation of curved open channel flows by 3D hydrodynamic model. *J. Hydraul. Eng.* **124** (7), 687–698.

Yang, Y. & Bai, Y. 2011 Three-dimensional numerical simulation of flow in successive bends. *J. Sediment Res.* **6**, 46–49 (in Chinese).

Zeng, J., Constantinescu, G. & Weber, L. 2008 A 3D non-hydrostatic model to predict flow and sediment transport in loose-bed channel bends. *J. Hydraul. Res.* **46** (3), 356–372.

Zhang, H. & Lv, X. 1993 *Bend Channel Hydraulics*. China WaterPower Press, Beijing (in Chinese).

Zhang, Z., Zhang, W., Zhai, Z. J. & Chen, Q. Y. 2007 Evaluation of various turbulence models in predicting airflow and turbulence in enclosed environments by CFD: Part 2 – comparison with experimental data from literature. *HVAC&R Res.* **13** (6), 871–886.

First received 30 September 2013; accepted in revised form 14 March 2014. Available online 16 April 2014